Measurement 222 (2023) 113614

Contents lists available at ScienceDirect

Measurement

journal homepage: www.elsevier.com/locate/measurement

Early rolling bearing fault diagnosis in induction motors based on on-rotor sensing vibrations

Zuolu Wang [a], Dawei Shi [a], Yuandong Xu [b], Dong Zhen [c], Fengshou Gu [a,*], Andrew D. Ball [a]

[a] Centre for Efficiency and Performance Engineering, University of Huddersfield, Huddersfield HD1 3DH, UK
[b] Hunan Provincial Key Laboratory of Health Maintenance for Mechanical Equipment, Hunan University of Science and Technology, Xiangtan, China
[c] School of Mechanical Engineering, Hebei University of Technology, Tianjin, China

ARTICLE INFO

Keywords:
On-rotor sensing
Vibration
Early fault diagnosis
Rolling bearing
Induction motor

ABSTRACT

The traditional on-house sensing (OHS) accelerometer for vibration measurements causes poor signal-to-noise ratio (SNR) and complicated fault modulations, which increases the difficulty and complexity for early bearing fault diagnosis. To overcome these challenges, this paper develops a wireless triaxial on-rotor sensing (ORS) system to largely improve the SNR and deduces fast Fourier transform (FFT) and Hilbert envelope analysis for accurate early rolling bearing fault diagnosis, which largely improves accuracy and efficiency for early fault diagnosis. First, the development of the ORS system for wireless vibration measurements is given. Second, the theoretical diagnostic relationships between dynamic ORS signals and rolling bearing faults are derived for FFT and Hilbert envelope analysis for the first time. Finally, the induction motor tests with outer and inner race faults successfully validate that both simple FFT and Hilbert envelope analysis can achieve more robust early rolling bearing fault diagnosis compared to OHS measurements.

1. Introduction

Rotating machines have gained widespread popularity in modern industries, such as compressors, pumps, conveyors, engines, induction motors, etc. [1,2]. The rolling bearing, as a key mechanical part of the rotating machine, plays a fundamental role in the safe and stable operation of the whole equipment [3,4]. However, the rolling bearings are easily vulnerable to failures owning to the long-time services with varying loads and severe working environments. It has been studied that the rolling bearing faults take up about 41 %–42 % of the whole number of induction motor failures [5]. Therefore, it is urgent to develop effective sensing technologies and methods for the early rolling bearing fault diagnosis, which is of great importance to guarantee stable operation, avoid catastrophic failure, and reduce economic losses.

Currently, a variety of sensing technologies have been applied to the condition monitoring and fault diagnosis of the rolling bearing, including vibration monitoring [6,7], acoustic emission monitoring [8], sound [9], thermal imaging [10], motor current [11] and so on. Vibration monitoring has been seen as the most reliable and effective technology for rolling bearing fault detections. The rolling bearing includes four common faults, such as outer race fault, inner race fault, rolling element fault, and cage faults. Once the fault occurs, a periodic transient impulse will be generated repetitively in the vibration signal, while the fault amplitudes are relatively lower and hence the fault features are weak, especially for the incipient rolling bearing faults [12]. The piezoelectric accelerometers have been widely used for vibration measurements in practice due to their low cost and high reliability. They highly depend on special wire connections for the data transmission and power supply. Therefore, they can only be mounted on a suitable position on the equipment to acquire the vibration signal. Consequently, the long transmission paths cause the low signal-to-noise ratio (SNR) of the measured vibration signal as the rolling bearings generally run under harsh conditions, and the fault features are easily corrupted in the external working noise. The complex transmission paths will also introduce more modulations in the measured signal. Moreover, the generated repetitively fault impulse features of the rolling bearing are not strictly periodic due to complex working conditions, such as the time-varying loads [13]. However, the second-order statistics present the periodic properties recognised by the cyclostationary theory [14,15]. The second-order cyclostationary properties make the typical fast Fourier transform (FFT) fails to detect the bearing fault [16,17]. Various challenges, including the multiple sources caused by the complex transmission path, weak fault feature and cyclostationary properties, make it difficult to extract the fault feature for the early rolling

* Corresponding author.
E-mail address: f.gu@hud.ac.uk (F. Gu).

https://doi.org/10.1016/j.measurement.2023.113614
Received 16 March 2023; Received in revised form 23 August 2023; Accepted 24 September 2023
Available online 29 September 2023

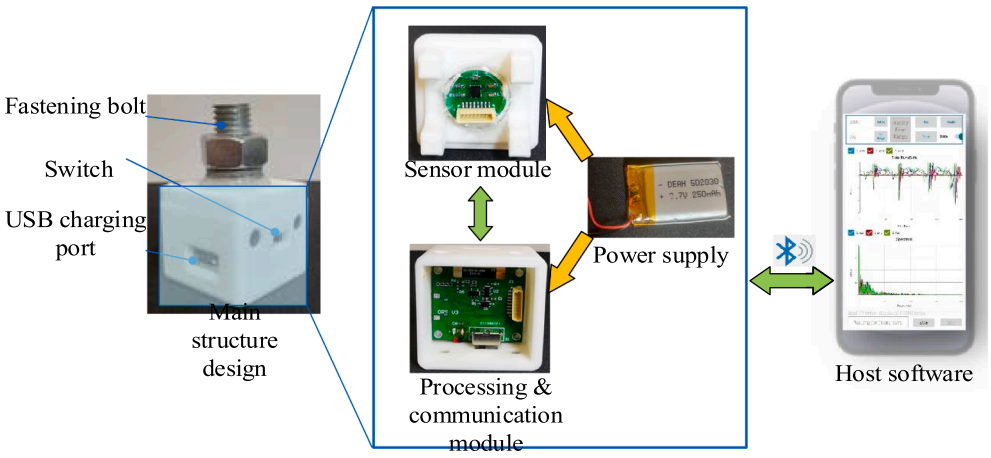

Fig. 1. ORS structure design.

bearing fault diagnosis.

A large amount of work has been dedicated to enhancing the weak fault feature in the measured vibration signals for the incipient rolling bearing fault detection. For example, the stochastic resonance (SR) [18,19] was proposed to specially enhance the weak fault feature with the assistance of the noise for the rotating machine fault detection. The turntable Q-factor wavelet transform (TQWT) [20] is an effective denoising method for the rolling bearing fault diagnosis. The variational mode decomposition (VMD) [21] can reduce the disturbance components from the background noise to extract fault characteristics. The orthogonal matching pursuit (OMP) [22] algorithm can be used to effectively match the periodic information related to fault features in the vibration signal. The cyclostationary analysis methods, such as cyclic modulation spectrum (CMS) and fast spectral correlation (Fast-SC) [23,24], aim to extract the periodically modulated fault features by considering the second-order cyclostationarity of the vibration signal. Although these methods have achieved high accuracy for rolling bearing fault detection, their applications in practice lead to large computational complexity.

Moreover, the wireless microelectromechanical system (MEMS) accelerometer has recently attracted much interest in rotor-mounted applications to improve the SNR of the collected vibration signal. Arebi et al. [25,26] utilized a wireless sensor to diagnose the misalignment of the rotating machine, which validated higher superior performance than the shaft encoder and the traditional wired sensor. Baghli et al. [27] used a wireless MEMS sensor to achieve accurate instantaneous torque and speed measurements on the rotating shaft. Jiménez et al. [28] developed a wireless MEMS sensor that can be mounted internally on the rotor and obtain the rotational speed of the rotor, which can help achieve the active control of the rotor vibration. Feng et al. [29] investigated the orthogonal outputs of an on-rotor MEMS accelerometer and achieved the condition monitoring of the reciprocating compressor based on the reconstructed tangential acceleration. Xu et al. [30 31] also validated the effectiveness of the rotor-mounted sensor for high SNR measurements and condition monitoring for rotating machines. These research works mentioned above focus on different applications based on wireless vibration measurements, which demonstrates that the rotor-mounted sensor can significantly improve the SNR of the vibration measurement. Furthermore, digital twin (DT) has become an emerging technology that has attracted much attention in the field of intelligent assessment of system degradation. DT technology can achieve the virtual representation of the real physical system based on the real-time interaction between the virtual model and the physical system through data collection and transmission [32]. A variety of research works have been conducted for the DT-based mechanical system degradation evaluation using the advanced modelling methods and vibration measurement [33–35]. The ORS technology with high SNR signal acquisition and wireless transmission can contribute to the high-quality modelling and real-time data interaction in the DT-based condition monitoring of the mechanical system.

Based on the above analysis, the complex non-stationary fault signatures of the rolling bearing make it very difficult for the early fault diagnosis due to the low SNR and complicated modulations when using traditional on-house sensing (OHS) for vibration measurements. However, there is no work to effectively clarify how to use the ORS for the rolling bearing fault diagnosis. Moreover, it is validated that the ORS-based vibration measurements can improve the SNR and show much potential in the DT-driven intelligent diagnosis of mechanical systems. Therefore, it is highly necessary to develop more advanced ORS and investigate their effective applications for the rolling bearing fault diagnosis.

Inspired by these studies, this paper proposes a wireless on-rotor sensing (ORS) system based on the MEMS accelerometer to improve the SNR and achieves an accurate and robust incipient fault diagnosis of the rolling bearing in the induction motor. The effectiveness of the developed ORS technology is validated by two induction motors with different outer and inner race faults severities. The main novelty and contributions of the proposed research are as follows:

1) The ORS system is developed into an integrated small entity so that it can be easily installed on the end of the rotor for non-invasive and stable vibration measurements.
2) The developed ORS largely improves the SNR of vibration collections than the traditional OHS.
3) The developed ORS makes the simple fast Fourier transform (FFT) possible for early fault diagnosis of the rolling bearing and the theoretical deduction is proposed for the first time.
4) The orthogonal outputs of the ORS system can be reconstructed into an analytical signal for easier and more robust application of the Hilbert transform for rolling bearing fault demodulation and detection.

The rest of the paper is organised as follows: Section 2 introduces the developed ORS system and illustrates the theoretical background for the rolling bearing fault diagnosis. The detailed experimental setup and procedures are presented in Section 3. Section 4 discusses the experimental results in validation of the ORS method, and the conclusions drawn from this work are shown in the final Section.

2. ORS system and theoretical background

2.1. ORS system

Thanks to the rapid development of the MEMS accelerometer, an

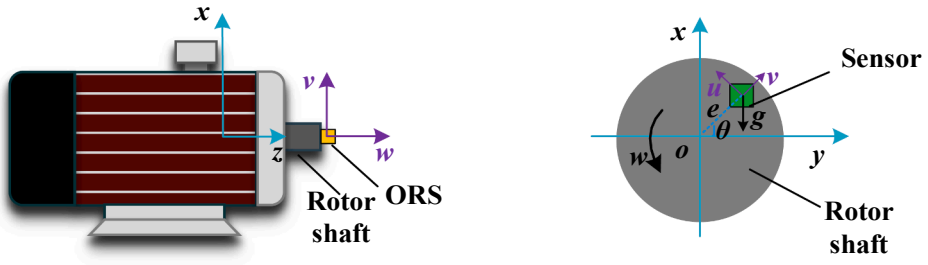

(a) ORS installation on the free end of the motor rotor.

(b) ORS sensor installation on the rotor shaft.

Fig. 2. The schematic diagram of the ORS installed on the motor rotor.

integrated wireless ORS system is developed in this paper. Fig. 1 illustrates the ORS structure design. All components are designed to be as small as possible, which allows them to be integrated into a small 3D-printed box with a dimension of 30 × 30 × 30 mm. A switch on the side of the box serves the purpose of controlling the power supply, and the USB charging port can be used to charge the system. The fastening bolt installed on the top of the box is used to connect the rotor of any rotating machine. The ORS system can rotate with the rotating shaft and achieve stable vibration signal acquisition.

The ORS system consists of four units, including a sensor module, processing module, communication module and power supply module. The 3.7 V lithium-ion battery is selected to power the other three modules. The vibration signal collected by the sensor module can be acquired by the processing module and then transmitted wirelessly to the host software through the communication module for the data processing, visualization, and storage. In particular, the ICM42688 MEMS accelerometer is selected as the sensor module for vibration measurements. It can allow the measurement of accelerations along three axes (*U*, *V* and *W*) with low energy consumption. The detection range is programmable, and the maximum range can reach up to ± 16 g (g is referred to as the acceleration of gravity and its value is $9.8m/s^2$). The sensor directly output the measurement of the vibration in the unit of g. Moreover, the data resolution of 18-bit can meet the different applications in practice. Currently, the sensor module has been fabricated to carry out the stable triaxial data acquisition with a sampling frequency between 0 and 4000 Hz. Moreover, the processing and communication modules are integrated into a single printed circuit board (PCB) to reduce installation space. The used nRF52840 processor is a good solution for controlling all the modules. It can communicate with the sensor module based on the onboard Serial Peripheral Interface (SPI) unit and request the digital signal from the sensor after ADC. In addition, the processor has Bluetooth low energy (BLE) module embedded to support the wireless data transmission with the host software. Therefore, an android APP was also developed to achieve wireless data transmission, visualization, and storage for further processing, as shown in Fig. 1.

In summary, various functions of the ORS have been upgraded compared to the old version, as mentioned in previous work [29 30]. For example, the current ORS is designed into a small integrated structure so that it can be flexibly mounted in the centre of the shaft as much as possible to achieve stable vibration measurements. Moreover, a new sensor called ICM42688 is fabricated to achieve the data acquisition with a high sampling frequency (4000 Hz) and resolution (18 bit). Furthermore, the improved data processing and transmission rate of the ORS ensures the stable transmission and real-time visualization of the data on the APP.

2.2. Theoretical background for rolling bearing fault diagnosis

The ORS is developed for the installation on the rotating rotor to improve the SNR for the condition monitoring and fault diagnosis of rotating machines. This section introduces its working principle for vibration signal measurements and even the rolling bearing fault diagnosis.

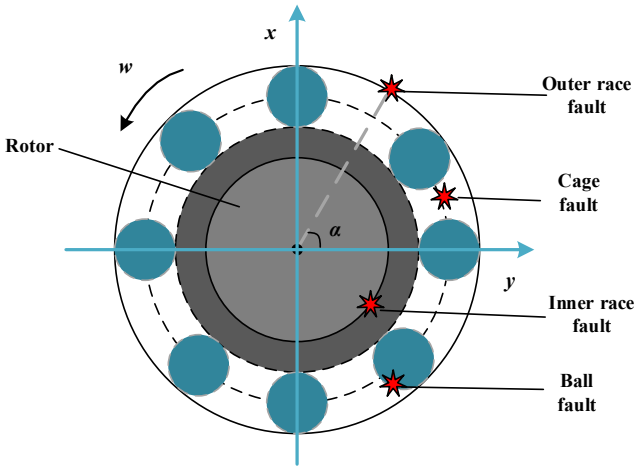

Fig. 3. Schematic diagram of the rolling bearing faults.

2.2.1. ORS installation and measurement

As shown in Fig. 2, the ORS system is designed to be easily installed on the end of the motor rotor, which allows for non-invasive condition monitoring of the rolling bearing. In order to avoid the influence of centrifugal force on the vibration measurement, the ORS system is mounted as centrally as possible. However, a small residual offset of *e* will be inevitable due to the installation error, as displayed in Fig. 2 (b) and should be taken into account in processing the signals.

The dynamic coordinate *u-v-w* is used to present the outputs of the triaxial MEMS accelerometer as the ORS system rotates with the rotor. They are responsible for the extraction of tangential, radial and axial vibrations, respectively. The *x-y-z* is a static coordinate that is fixed on the motor and can be the reference of the rotating coordinate *u-v-w*. According to the geometric relationship as shown in Fig. 2, the tangential (u) and radial (v) responses can be expressed as follows:

$$u(t) = -y(t)\sin(\omega t) + x(t)\cos(\omega t) - g\cos(\omega t) \tag{1}$$

$$v(t) = y(t)\cos(\omega t) + x(t)\sin(\omega t) - g\sin(\omega t) + \omega^2 e \tag{2}$$

where ω presents the rotational angular velocity of the motor rotor. g is the gravity acceleration. $x(t)$ and $y(t)$ stand for vertical and horizontal vibration, respectively. The $\omega^2 e$ can be neglected as $e \ll 1$.

The rolling element bearing consists of outer race fault, inner race fault, rolling element fault, and cage fault. As illustrated in Fig. 3, the

bearing rotates with the motor rotor with ω. These faults can generate different responses in different directions. Taking the outer race fault as an example, there is an angle α between the fault location and the y-axis. Therefore, two accelerometers are required to be installed vertically and horizontally to capture more fault information for fault diagnosis. Generally, they are statically installed on the shell of the motor, thus easily causing low SNR. In contrast, the ORS system embedded with the triaxial MEMS accelerometer can be installed concentrically on the shaft end, which not only improves the SNR, but also accurately captures the fault content based on the orthogonal outputs as shown in Fig. 2.

2.2.2. Fast Fourier transform-based analysis

The developed ORS system can acquire the vibration signal with higher SNR, and thus computationally efficient fast Fourier transform (FFT) can be an effective method for the rolling bearing fault feature extraction and detection. Four main components in the rolling bearing present different behaviours when rotating with the rotor. For example, the outer race remains stationary when running, the inner race rotates coaxially with the rotor with ω, while both the rolling element and the cage rotate themselves with different speed from the motor rotor. As results, various faults can appear in the different conditions and generate different responses in the dynamic axis of u-w.

On the one hand, the fault characteristic frequencies can exist in the form of harmonics in the frequency domain, such as the outer race faults. Therefore, the responses in x and y directions can be described as follows:

$$x_h(t) = \sum_{l=1}^{\infty} A_x(l)\cos\left(l\omega_f t\right)\cos\omega' t + \sum_{l=1}^{\infty} A_y(l)sin\left(l\omega_f t\right)\sin\omega' t \tag{3}$$

$$y_h(t) = -\sum_{l=1}^{\infty} A_x(l)\cos\left(l\omega_f t\right)\sin\omega' t + \sum_{l=1}^{\infty} A_y(l)sin\left(l\omega_f t\right)cos\omega' t \tag{4}$$

where $x_h(t)$ and $y_h(t)$ denote the fault responses in the form of harmonics in x and y directions, respectively. ω_f stands for the fault frequency. $A_x(l)$ and $A_y(l)$ denote the amplitudes of the fault frequency in x-y axis. ω' present the rotating speed of the fault. In terms of the outer race fault, the $\omega' = 0$ so that the response $x_o(t)$ and $y_o(t)$ for the outer race fault in x and y directions can be expressed as:

$$x_o(t) = \sum_{l=1}^{\infty} A_x(l)\cos\left(l\omega_f t\right) \tag{5}$$

$$y_o(t) = \sum_{l=1}^{\infty} A_y(l)sin\left(l\omega_f t\right) \tag{6}$$

According to the Eqs. (1) and (2), the responses $u_o(t)$ and $v_o(t)$ for the outer race fault in u and v directions hence can be calculated as Eq. (7) and Eq. (8). It can be seen that $u_o(t)$ and $v_o(t)$ include frequency components $l\omega_f + \omega$ and $l\omega_f - \omega$ related to the fault frequency, which shows that the fault frequency occurs in the form of sidebands, and they modulate on the rotating frequency.

$$u_o(t) = \frac{1}{2}\sum_{l=1}^{\infty}[A_x(l) - A_y(l)]\left\{\cos\left[\left(l\omega_f + \omega\right)t\right]\right\} + \frac{1}{2}\sum_{l=1}^{\infty}[A_x(l) + A_y(l)]\left\{\cos\left[\left(l\omega_f - \omega\right)t\right]\right\} - g\cos(\omega t) \tag{7}$$

$$v_o(t) = \frac{1}{2}\sum_{l=1}^{\infty}[A_y(l) - A_x(l)]\left\{\cos\left[\left(l\omega_f - \omega\right)t - \frac{\pi}{2}\right]\right\} + \frac{1}{2}\sum_{l=1}^{\infty}[A_y(l) + A_x(l)]\left\{\cos\left[\left(l\omega_f + \omega\right)t - \frac{\pi}{2}\right]\right\} - g\cos\left(\omega t - \frac{\pi}{2}\right) \tag{8}$$

On the other hand, the defect frequencies occur in the form of modulations, such as the inner race fault, ball fault, and cage fault. Therefore, the general expressions of $x(t)$ and $y(t)$ can be as follows:

$$x_m(t) = \sum_{l=1}^{\infty} A_x(l)\cos\left(l\omega_f t\right)[1 + B_x(l)\cos(\omega t)]\cos\omega' t + \sum_{l=1}^{\infty} A_y(l)sin(l\omega t)[1 + B_y(l)\sin(\omega t)]\sin\omega' t \tag{9}$$

$$y_m(t) = -\sum_{l=1}^{\infty} A_x(l)\cos\left(l\omega_f t\right)[1 + B_x(l)\cos(\omega t)]\sin\omega' t + \sum_{l=1}^{\infty} A_y(l)sin(l\omega t)[1 + B_y(l)\sin(\omega t)]cos\omega' t \tag{10}$$

Where $x_m(t)$ and $y_m(t)$ represent the fault responses in the form of modulations in x and y directions. The ω' is equal to ω for the inner race fault as it rotates with the motor rotor. Similarly, the inner race fault responses $u_i(t)$ and $v_i(t)$ in u and v directions can be obtained in Eq. (11) and Eq. (12). In addition to the sidebands $l\omega_f + \omega$ and $l\omega_f - \omega$, the inner race fault also includes the separate fault frequency $l\omega_f$ in the frequency domain.

$$u_i(t) = \sum_{l=1}^{\infty} A_x(l)\cos\left(l\omega_f t\right) + \frac{1}{2}\sum_{l=1}^{\infty} A_x(l)B_x(l)\{\cos[(l\omega_f + \omega)t] + \cos[(l\omega_f - \omega)t]\} - g\cos(\omega t) \tag{11}$$

$$v_i(t) = \sum_{l=1}^{\infty} A_y(l)\cos\left(l\omega_f t - \frac{\pi}{2}\right) + \frac{1}{2}\sum_{l=1}^{\infty} A_y(l)B_y(l)\{\cos[(l\omega_f - \omega)t] - \cos[(l\omega_f + \omega)t]\} - g\cos\left(\omega t - \frac{\pi}{2}\right) \tag{12}$$

The above theoretical analysis can support the rolling bearing fault diagnosis based on the FFT method. This paper especially focuses on the detections of inner race fault and outer race fault. In the case of the ball fault and cage fault, their slippage will result in $\omega' \neq \omega$, and the vibration responses in u and v directions are given as follows.

$$\begin{aligned} u_{b,c}(t) = {} & \frac{1}{2}\sum_{l=1}^{\infty}[A_x(l)+A_y(l)] \bullet \cos\left[\left(l\omega_f - \omega' + \omega\right)t\right] + \frac{1}{4}\sum_{l=1}^{\infty}[A_x(l) \\ & \bullet B_x(l) + A_y(l) \bullet B_y(l)]\{\cos[(l\omega_f - \omega' + 2\omega)t] + \cos[(l\omega_f \\ & - \omega')t]\} + \frac{1}{2}\sum_{l=1}^{\infty}[A_x(l) - A_y(l)] \bullet \cos\left[\left(l\omega_f + \omega' - \omega\right)t\right] \\ & + \frac{1}{4}\sum_{l=1}^{\infty}[A_x(l) \bullet B_x(l) - A_y(l) \bullet B_y(l)]\{\cos[(l\omega_f + \omega')t] + \cos[(l\omega_f \\ & - \omega' - 2\omega)t]\} - g \bullet \cos(\omega t) \end{aligned} \tag{13}$$

$$\begin{aligned} v_{b,c}(t) = {} & \frac{1}{2}\sum_{l=1}^{\infty}[A_x(l)+A_y(l)] \bullet \cos\left[\left(l\omega_f - \omega' + \omega\right)t - \frac{\pi}{2}\right] + \frac{1}{4}\sum_{l=1}^{\infty}[A_x(l) \\ & \bullet B_x(l)+A_y(l) \bullet B_y(l)]\{\cos[(l\omega_f - \omega')t] - \cos[(l\omega_f - \omega' \\ & + 2\omega)t]\} + \frac{1}{2}\sum_{l=1}^{\infty}[A_y(l)-A_x(l)] \bullet \cos\left[\left(l\omega_f + \omega' \right.\right. \\ & \left.\left. - \omega\right)t - \frac{\pi}{2}\right] + \frac{1}{4}\sum_{k=1}^{\infty}[A_y(k) \bullet B_y(k)-A_x(k) \bullet B_x(k)]\{\cos[(l\omega_f + \omega' \\ & - 2\omega)t] - \cos[(l\omega_f + \omega')t] - g \bullet \cos\left(\omega t - \frac{\pi}{2}\right) \end{aligned} \tag{14}$$

where $u_{b,c}(t)$ and $v_{b,c}(t)$ stand for the response for ball fault and cage fault in u and v directions. To effectively capture the fault feature, the measured vibration signals by two orthogonal axes can be reconstructed to obtain the joint response in the frequency domain. The applications for traditional on-house sensing (OHS) and ORS are shown as follows:

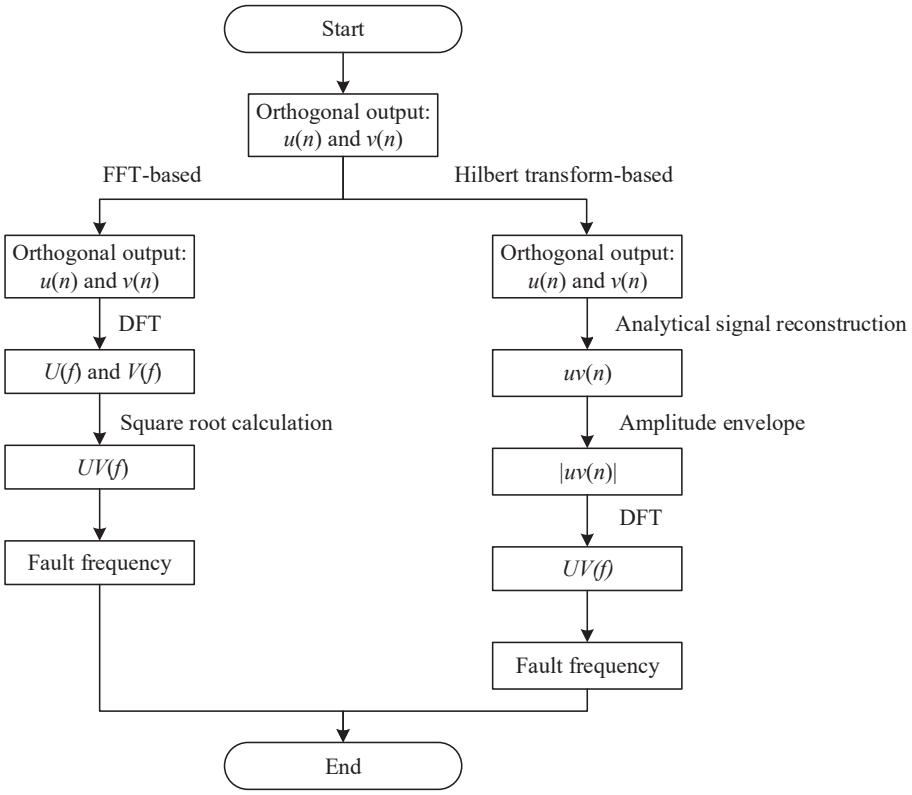

Fig. 4. The flowchart of FFT and Hilbert transform-based rolling bearing fault diagnosis using ORS.

1) OHS

For the traditional measurement of OHS, the signals $x'(t)$ and $y'(t)$ can be obtained in vertical and horizontal directions, respectively. Therefore, the joint response $XY(f)$ in the frequency domain can be calculated as follows:

$$XY(f) = \sqrt{X(f)^2 + Y(f)^2} \tag{15}$$

$$X(f) = DFT(x'(n)) \tag{16}$$

$$Y(f) = DFT(y'(n)) \tag{17}$$

where $x'(n)$ and $y'(n)$ present the discrete forms of $x'(t)$ and $y'(t)$, respectively. DFT denotes the discrete Fourier transform.

2) ORS

Similarly, the joint response $UV(f)$ of $u(t)$ and $v(t)$ collected by the ORS system can be expressed as follows:

$$UV(f) = \sqrt{U(f)^2 + V(f)^2} \tag{18}$$

$$U(f) = DFT(u(n)) \tag{19}$$

$$V(f) = DFT(v(n)) \tag{20}$$

where $u(n)$ and $v(n)$ present the discrete forms of $u(t)$ and $v(t)$, respectively.

2.2.3. Hilbert transform-based analysis

In addition to the FFT-based method, the Hilbert envelope analysis method is efficient and effective for processing the non-stationary weak fault signal for the fault feature extraction and diagnosis of the rolling bearing in the early stage. It has been widely used for condition monitoring and fault diagnosis in rotating machines [36,37]. The Hilbert envelope of the signal $s(n)$ is theoretically calculated as follows:

$$s_a(n) = s(n) + js_h(n) \tag{21}$$

where $s_a(n)$ is the reconstructed analytical signal and $s_h(n)$ stands for the Hilbert transform of the $s(n)$ and it is given as

$$s_h(n) = IDFT(S_h(f)) \tag{22}$$

$$S_h(f) = \begin{cases} +jS(f) f < 0 \\ -jS(f) f > 0 \end{cases} \tag{23}$$

$$S(f) = DFT(s(n)) \tag{24}$$

where IDFT is the inverse DFT. Therefore, the amplitude envelope $|s_a(n)|$ can be calculated as follows:

$$|s_a(n)| = \sqrt{s^2(n) + s_h^2(n)} \tag{25}$$

The orthogonal outputs obtained by two accelerometers can be used to reconstruct the analytical signal for envelope analysis. In the ORS system, the orthogonal outputs $u(n)$ and $v(n)$ have a phase difference of $\pi/2$. Thus the $v(n)$ can be seen as the Hilbert transform of $u(n)$ theoretically. Therefore, the Hilbert envelope analysis can be given as follows:

$$uv(n) = u(n) + jv(n) \tag{26}$$

$$|uv(n)| = \sqrt{u^2(n) + v^2(n)} \tag{27}$$

$$UV(f) = DFT(|uv(n)|) \tag{28}$$

where $|uv(n)|$ stands for amplitude envelope and $UV(f)$ is the DFT of $|uv(n)|$. It is believed that the ORS system can achieve a more convenient Hilbert envelope analysis for fault demodulation and feature extraction.

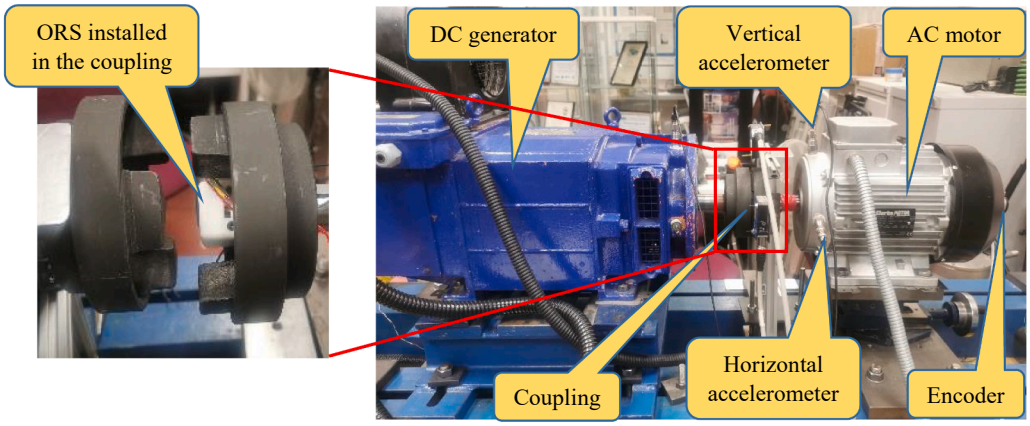

Fig. 5. Induction motor test rig.

Table 1
AC motor specification.

Type	Specification
Motor model	112 M/4
Power	4.4 kW, 3 phase
Frequency	50 Hz
Rated speed	1420 rpm

Based on the theoretical deduction for both FFT and Hilbert transform, the early fault diagnosis of the rolling bearing based on the orthogonal output of the ORS measurement can be implemented by the procedures as shown in Fig. 4.

3. Experiments

The induction motor test benches are carried out to demonstrate the effectiveness of the developed ORS system for the condition monitoring and fault diagnosis of the rolling element bearing in induction motors. Fig. 5 shows the setup of the induction motor test rig. It consists of an AC induction motor as the driven source, a DC generator as the loader, a coupling as the flexible connection between the AC motor and the DC loader, and an encoder that is mounted at the free end of the motor for rotating speed recording. Table 1 shows the specifications of the targeted AC induction motor. Two single-axis accelerometers are orthogonally installed on the shell of the motor to acquire the vertical and horizontal vibration responses. The ORS system is fixed on the rotor end of the motor, and it is placed inside the flexible coupling for vibration measurements.

In the test, two induction motors with compound inner race fault and outer race fault are used to validate the performance of the ORS system for rolling bearing fault diagnosis. As shown in Fig. 6, they are marked as Motor #1 and Motor #2. There are no specially designed rolling bearing failures in these two motors, while they present different levels of outer and inner race faults. It is assumed that damages are caused by the rotor eccentricity and bearing clearances due to manufacturing errors and long-time services. Particularly, Motor #2 served longer on the test bench than Motor #1, and hence it is believed that Motor #2 can present more severe failure of the rolling bearing. Table 2 displays the specification of the rolling bearing used in the motor.

According to the given specifications of the rolling bearing, the outer race fault f_o and inner race fault f_i can be theoretically calculated as follows:

$$f_o = \frac{Nf_r}{2}\left(1 - \frac{D}{d}cos\theta\right) \tag{29}$$

$$f_i = \frac{Nf_r}{2}\left(1 + \frac{D}{d}cos\theta\right) \tag{30}$$

Table 2
Specifications of the rolling bearing.

Parameters	Ball diameter	Pitch circle diameter	Number of balls	Contract angle
Value	9.53 mm	46.4 mm	9	0°

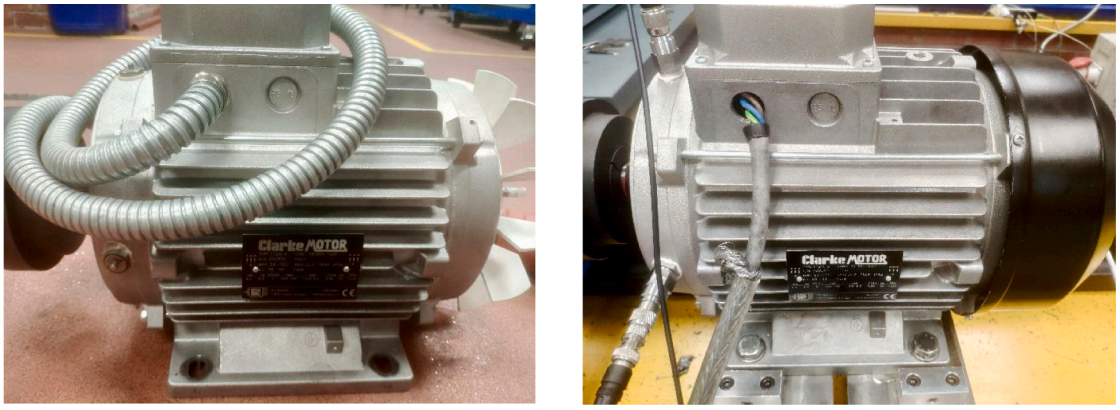

(a) AC Motor #1. (b) AC Motor #2.

Fig. 6. Two tested induction motors.

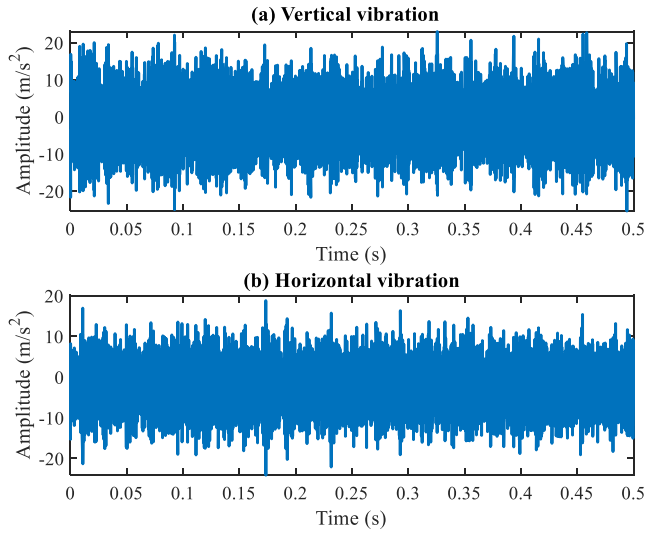

Fig. 7. Time-domain vibration waveform obtained by OHS in (a) vertical and (b) horizontal directions.

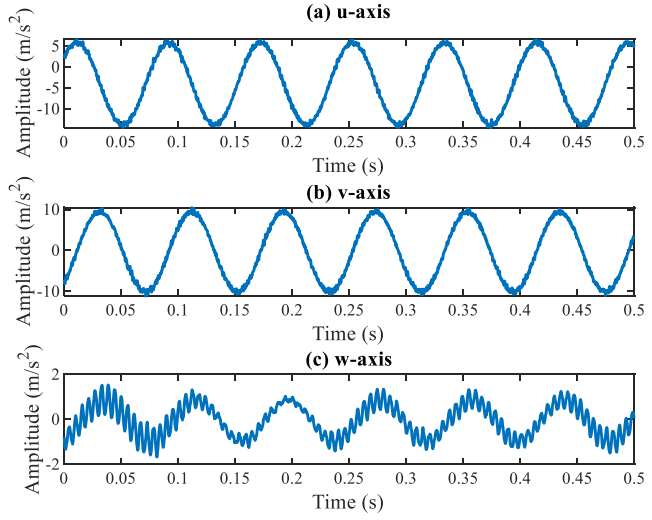

Fig. 8. Time-domain vibration waveform obtained by ORS in (a) u, (b) v, and (c) w axis.

where f_r presents the rotating frequency, N denotes the number of balls, θ is the contact angle, and D and d stand for the ball diameter and pitch circle diameter, respectively.

Two motors are tested under 0 % load but at different running speeds, including 50 %, 75 %, and 100 % of the full speed, for rolling bearing fault diagnosis. The high-speed acquisition system YE6232B with a sampling frequency of 96 kHz was used to acquire the vibration signals obtained by vertical and horizontal accelerometers. For the ORS system, the sampling frequency and the test range are 4000 Hz and 16 g, respectively. The vibration signals can be continuously acquired and wirelessly transmitted to the smartphone. A 40-second signal is acquired to ensure accurate fault feature extraction and diagnosis.

4. Results and discussion

4.1. SNR analysis

Taking Motor #1 working under the 50 % speed as the example, Fig. 7 and Fig. 8 display the vibration signals measured by OHS on both vertical and horizontal vibrations and ORS on three axes. It can be seen from Fig. 7 that vibration signals measured by traditional accelerometers present large oscillations and background noise both in vertical and horizontal directions due to complex transmission paths. This increases the difficulty of fault demodulation and feature extraction. Fig. 8 (a) and Fig. 8 (b) show the rotor vibration in radial and tangential directions. It can be seen that they are not overwhelmed by the noise and present more content of the rotating speed. In particular, the vibration amplitudes in both directions have a difference of $\pi/2$, which helps reconstruct the analytical signal for more convenient Hilbert envelope analysis. As shown in Fig. 8 (c), the vibration obtained at the w-axis presents a relatively smaller amplitude as it measures the vibration signal at the axial direction. Therefore, only the vibrations measured by the u and v axis are used for the bearing fault diagnosis. Compared to the OHS system, the ORS system can considerably improve the SNR of the measured signals, which facilitates fault feature extraction and diagnosis.

To further quantify the SNR improvement of the developed ORS system, the SNR is calculated using the energy of useful signals and noise in which the key frequency components, including rotating frequency, fault frequency and their harmonics, are extracted for the useful signal, and the rest is seen as the noise. Fig. 9 compares the calculated SNR of the vibration signal collected by ORS and OHS. Obviously, the developed ORS can achieve significantly enhance the SNR of the collected vibration signal compared to the traditional OHS method. Whether for Motor 1# or Motor 2#, it can be seen that the ORS can achieve high-SNR

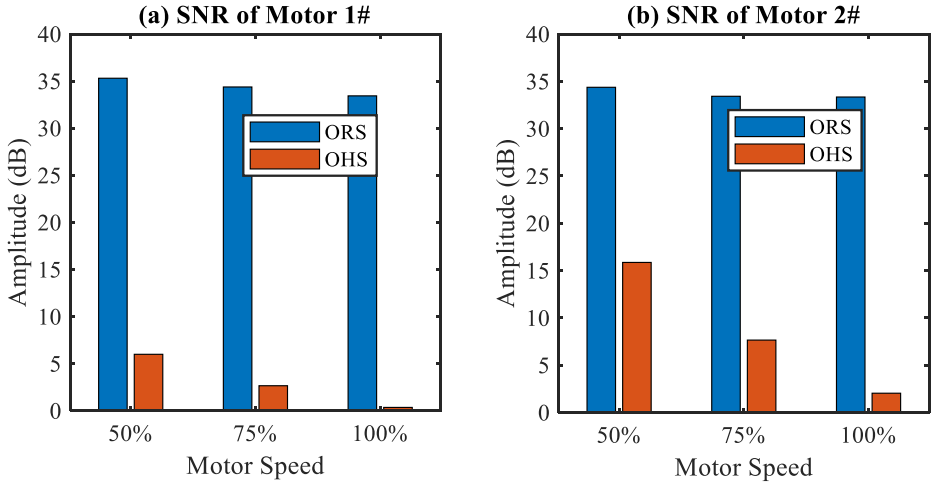

Fig. 9. Comparison of SNR between ORS and OHS for vibration signal measurements.

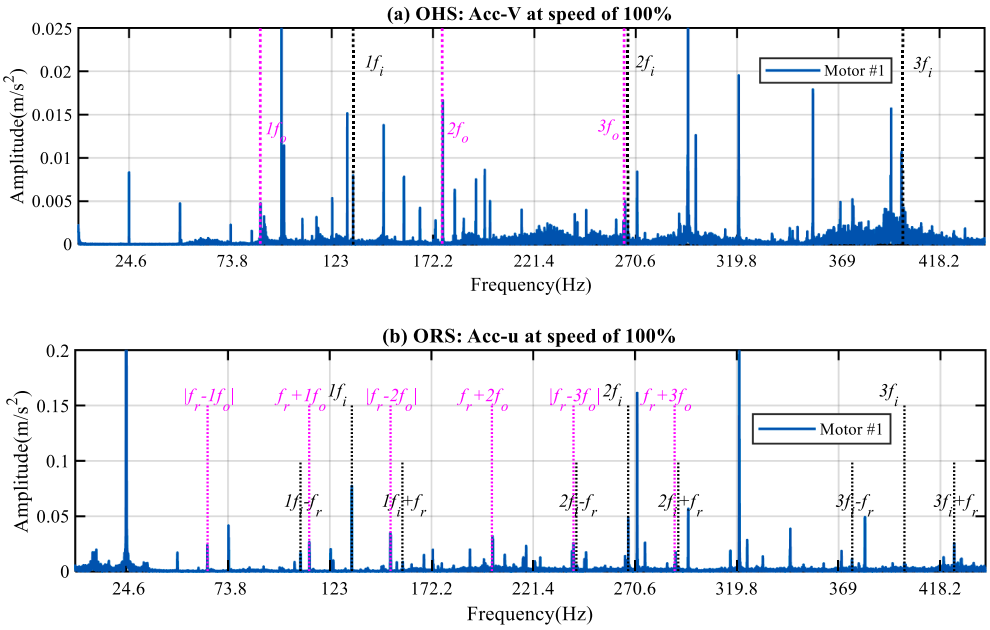

Fig. 10. Spectrum of the rolling bearing vibration at speed of 100%: (a) obtained by OHS at vertical direction and (b) obtained by ORS at *u* axis.

Table 3
Rotating frequencies and fault frequencies of the rolling bearing under different working conditions.

Speed (%)	50	75	100
Rotating frequency (Hz)	12.4	18.6	24.6
Outer race fault frequency f_o (Hz)	44.4	66.5	88.0
Inner race fault frequency f_i (Hz)	67.3	100.9	133.4

vibration collection under different rotating speeds. For example, the improved SNRs by ORS are 29.3 dB, 30.7 dB, and 33.1 dB, respectively.

4.2. FFT analysis

As mentioned previously, the developed ORS system enables vibration measurements with high SNR. This makes the simple FFT analysis effective for early rolling bearing fault detection, which helps achieve a more efficient early fault diagnosis of the rolling bearing. To illustrate the performance of the ORS system, Fig. 10 shows the FFT results using the measured signals by OHS and ORS in the case of Motor #1 working

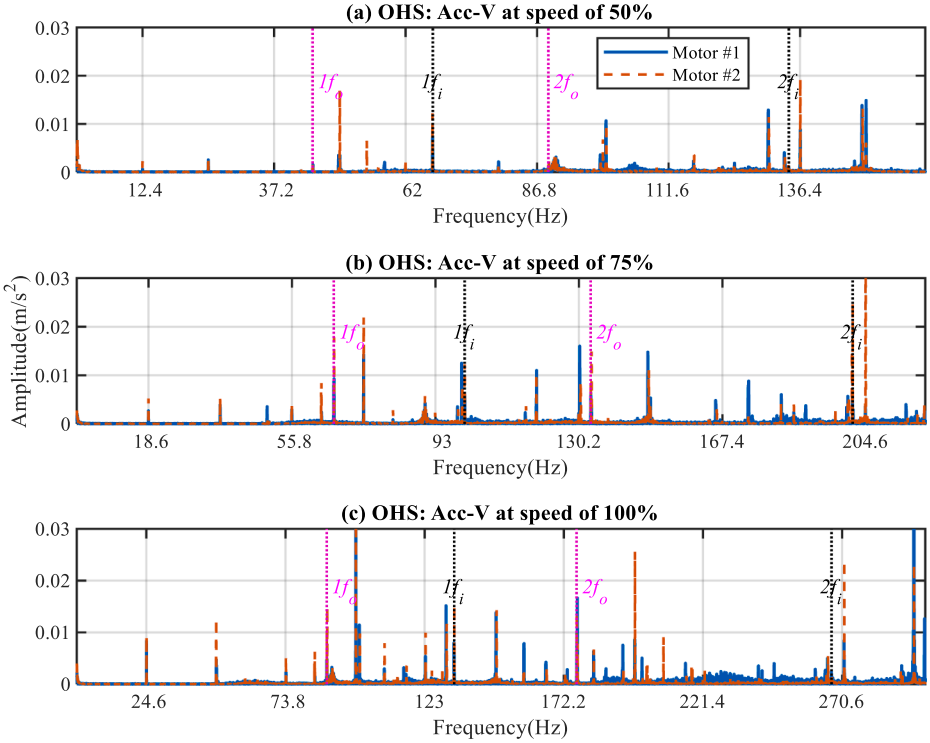

Fig. 11. OHS spectrum of the vertical vibration at speeds of (a) 50%, (b) 75%, and (c) 100%.

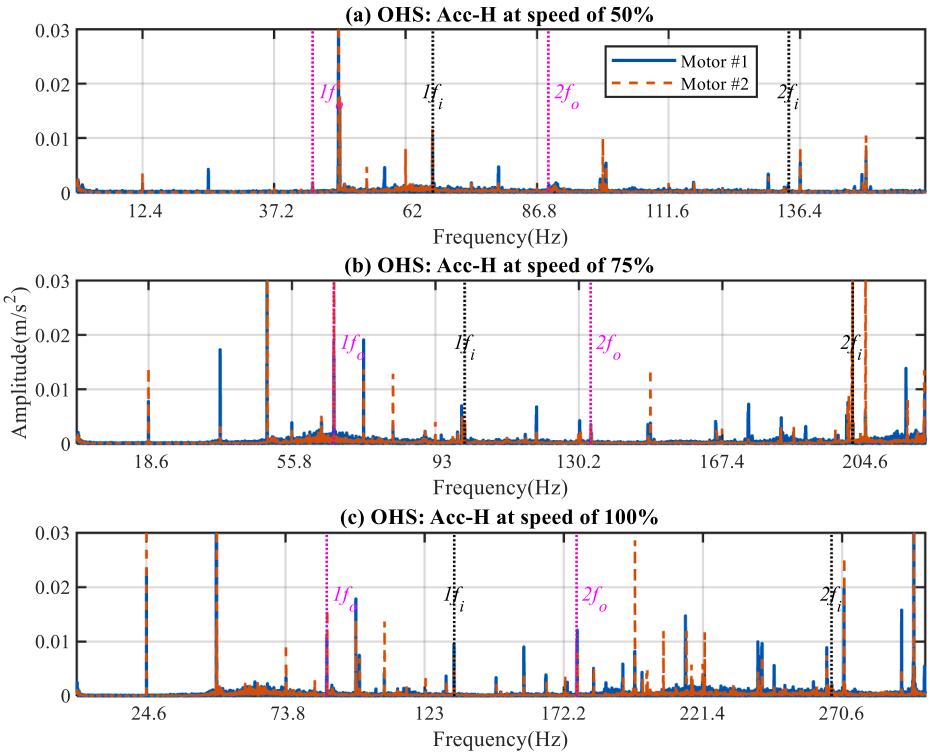

Fig. 12. OHS spectrum of the horizontal vibration at speeds of (a) 50%, (b) 75%, and (c) 100%.

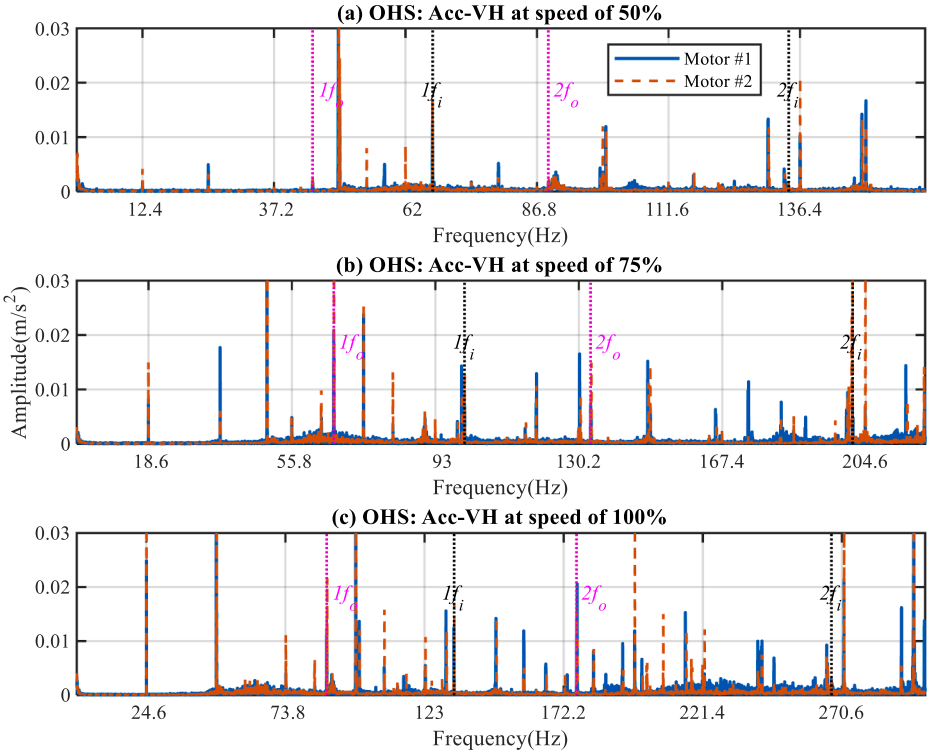

Fig. 13. OHS spectrum of the combined vertical and horizontal vibration at speeds of (a) 50%, (b) 75%, and (c) 100%.

under 100 % speed. Based on the theoretical calculations of the inner and outer race fault frequencies, the OHS spectrum presents the fault harmonics, as shown in Fig. 10 (a). According to the theoretical derivation in Section 2.2, the identical detected results are obtained in the FFT spectrum. As shown in Fig. 10 (b), the outer race fault appears in the spectrum in the sidebands around the fault characteristic frequency since the rotating frequency f_r is modulated on the outer race fault characteristic frequency f_o. Moreover, the inner race fault shows both the fault characteristic frequency f_i and its two sidebands which are caused by the rotating frequency modulation on inner race fault

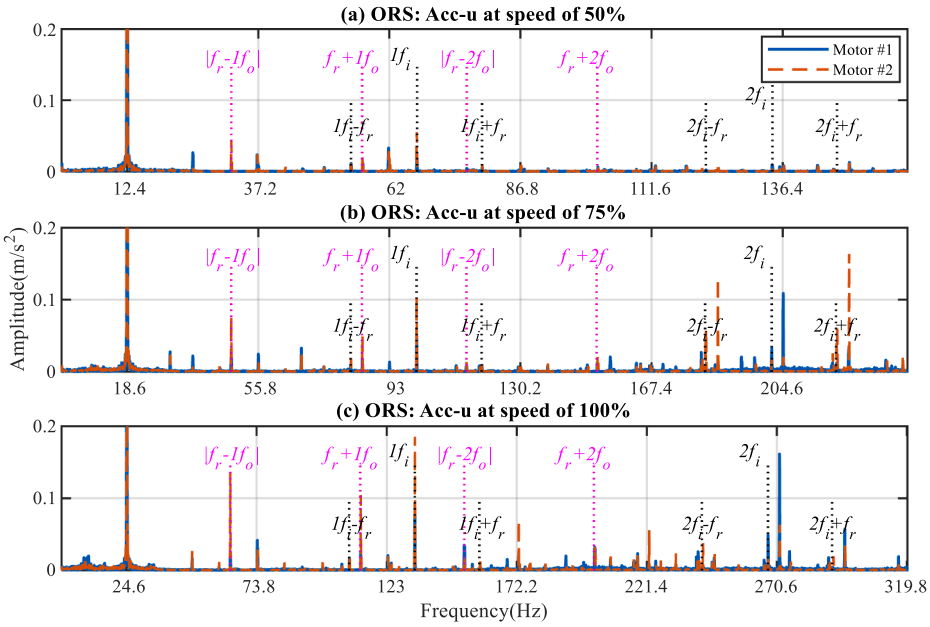

Fig. 14. ORS spectrum of the *u*-axis vibration at speeds of (a) 50%, (b) 75%, and (c) 100%.

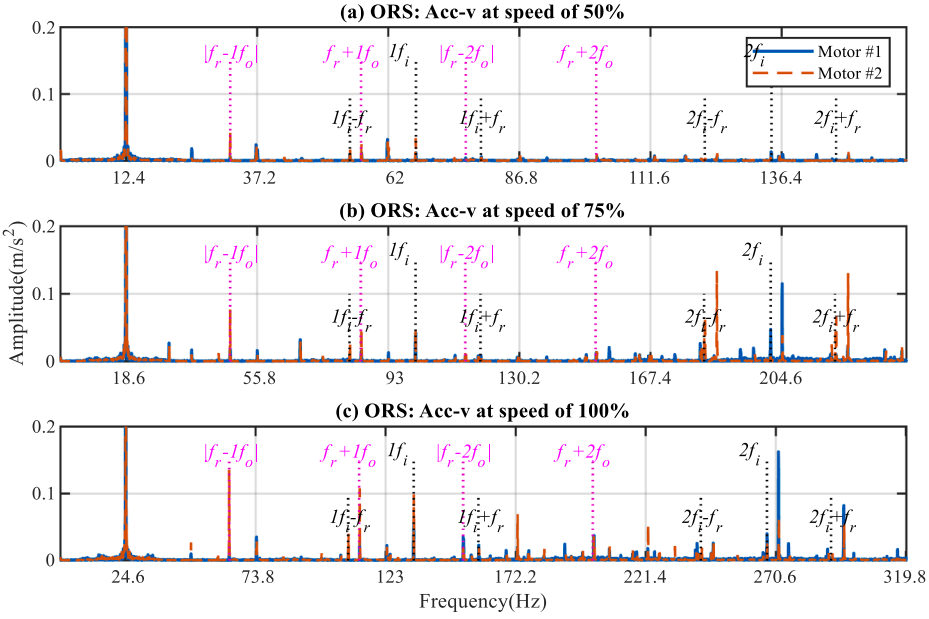

Fig. 15. ORS spectrum of the *v*-axis vibration at speeds of (a) 50%, (b) 75%, and (c) 100%.

frequency f_i. Whether the outer race fault or the inner race fault, the related fault frequencies can be obviously seen in the spectrum, which validates the effectiveness of the developed ORS system for the rolling bearing fault diagnosis based on the FFT analysis.

To further compare the performance of the ORS and OHS for the rolling bearing fault diagnosis, the measured vibration signals of two motors working under different conditions are analysed based on the FFT algorithm. Table 3 displays the rotating frequencies and fault frequencies of the rolling bearing at different working conditions. Fig. 11, Fig. 12, and Fig. 13 show the FFT spectrum of two motors based on the vertical, horizontal, and combined vertical and horizontal OHS vibration, respectively. It can be seen that the OHS vibration is able to detect the outer and inner race faults based on the FFT analysis. However, the spectrum exhibits many irrelevant interference components due to the measurement of a large amount of noise by the OHS method. As a consequence, the amplitudes of the fault characteristic frequencies are too small in the spectrum, especially for low operating load conditions, such as 50 % speed. As shown in Fig. 11 (a) and Fig. 12 (a), it is difficult to extract the outer race fault feature. The theoretical analysis has explained that the FFT analysis based on the orthogonal vibration measurements can achieve more effective fault feature extraction and diagnosis. It can be seen from Fig. 13 that the extracted fault frequency amplitudes are higher than that analysed by the single vertical or horizontal vibration signal. Although the combined vertical and horizontal accelerometers can facilitate fault diagnosis, it undoubtedly increases the measurement cost.

Moreover, Fig. 14, Fig. 15 and Fig. 16 present the FFT spectrum for the rolling bearing fault diagnosis obtained by the ORS measurement at the *u* axis, *v* axis and *uv* axis. Compared to the OHS measurement, it can be seen that the FFT spectrum obtained by the ORS can provide a more

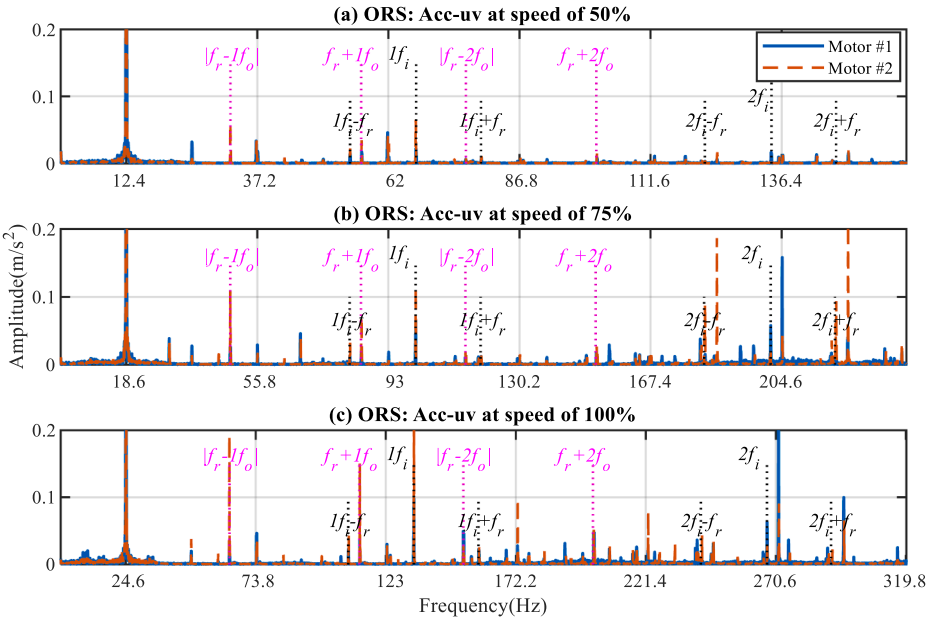

Fig. 16. ORS spectrum of the *uv*-axis vibration at speeds of (a) 50%, (b) 75%, and (c) 100%.

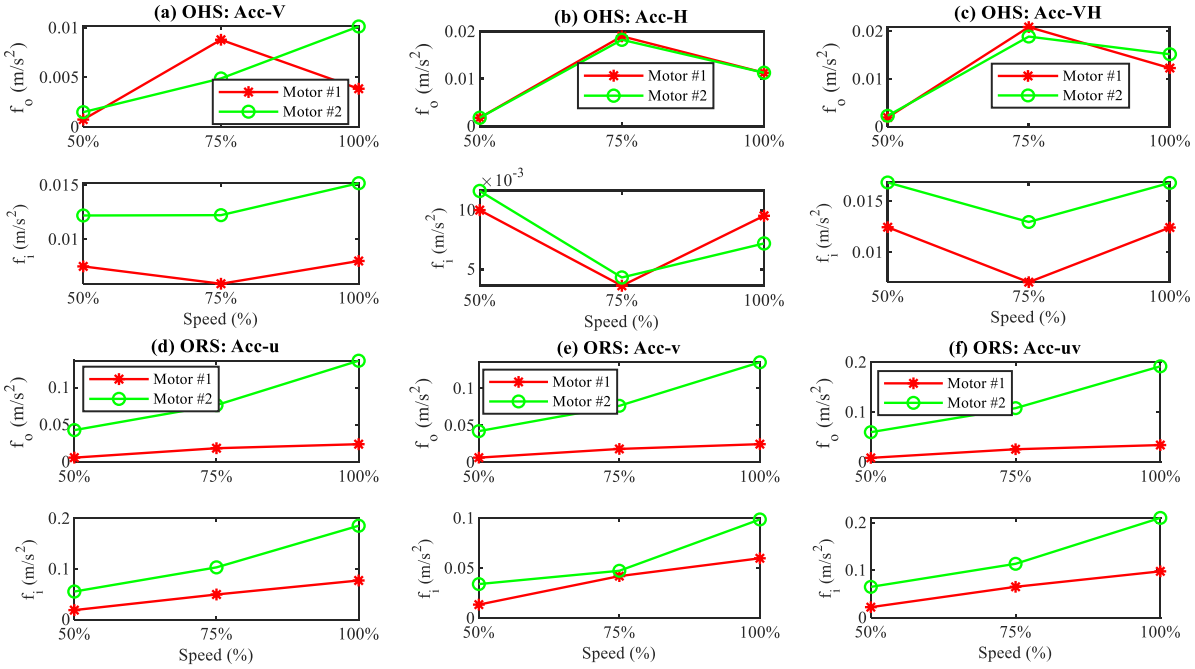

Fig. 17. Amplitudes of rolling bearing outer race ($|f_r - 1f_o|$) and inner race ($1f_i$) fault frequencies of two motors under different working conditions obtained by (a) OHS at V axis, (b) OHS at H axis, (c) OHS at VH axis, (d) ORS at *u* axis, (e) ORS at *v* axis, and (f) ORS at *uv* axis.

robust rolling bearing fault feature extraction and detection. On the one hand, there are no more interference components found in the spectrum. On the other hand, the extracted fault frequency amplitudes are significantly higher than that obtained by the OHS analysis. In addition, the FFT spectrum obtained by the orthogonal measurement (u-axis and v-axis), as illustrated in Fig. 16, can more effectively enhance the fault feature compared to the single u-axis, v-axis and even the OHS analysis.

A lot of researchers have dedicated to the numerical studies of rolling bearing faults, and it is validated that the severity of outer race fault or inner race fault shows an upward trend with increasing of motor speeds [38,39]. This can be used to examine the performance of the developed ORS method for the robust rolling bearing fault diagnosis. The fault frequency amplitudes are adopted to quantify the severity of the outer and inner race faults. Therefore, Fig. 17 compares the outer and inner face fault frequency amplitudes obtained by OHS and ORS using vibration measurements in different directions. In particular, Fig. 17 (a), (b), and (c) show the fault frequency amplitudes obtained by the OHS method. It can be seen from Fig. 17 (c) that the joint response can provide a more effective diagnosis with higher amplitudes compared to results obtained by OHS in the vertical or horizontal direction. However, the OHS-based detection method cannot show the variation that the bearing fault severity increases with the increase in speed. Moreover, it is not able to distinguish two different motors. Fig. 17 (d), (e), and (f) exhibit the detected results based on the developed ORS method. It is

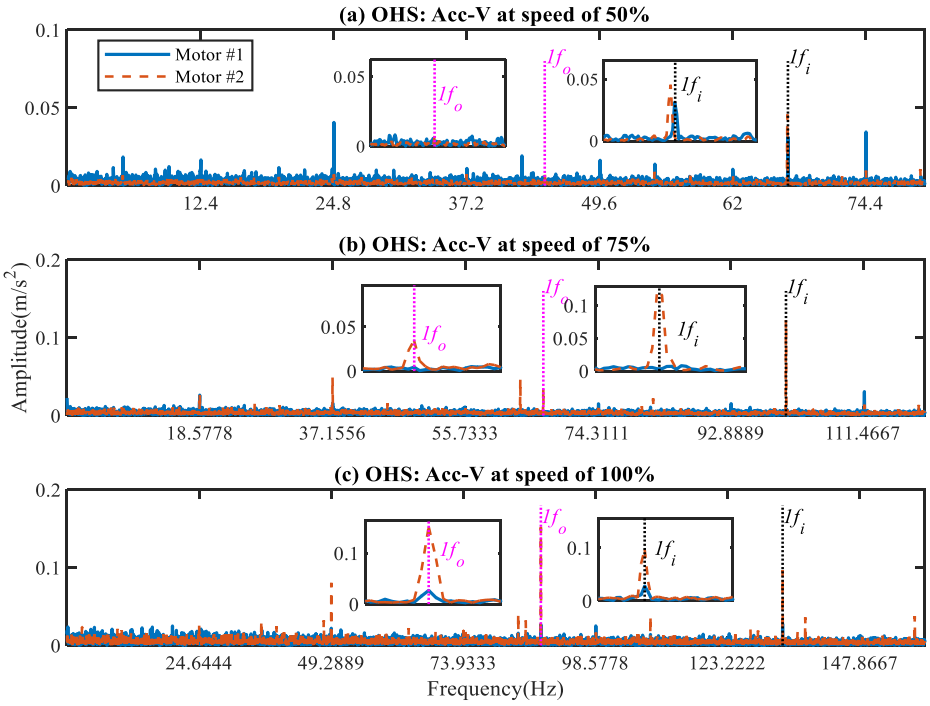

Fig. 18. Hilbert envelope spectrum based on the vertical OHS vibration at (a) 50%, (b) 75%, and (c) 100%.

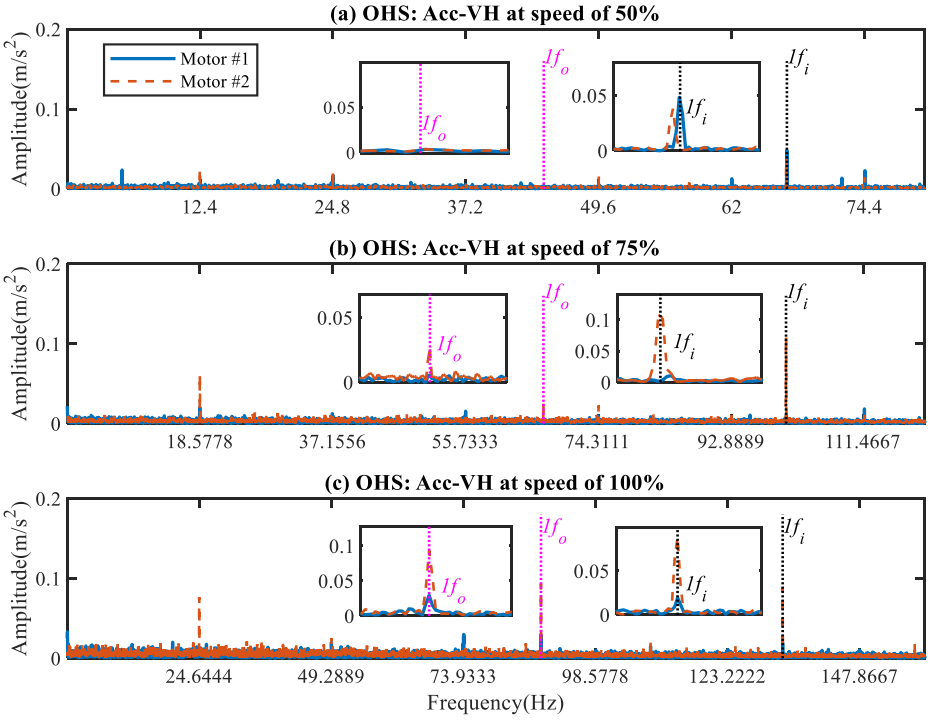

Fig. 19. Hilbert envelope spectrum of based on the vertical and horizontal OHS vibration at (a) 50%, (b) 75%, and (c) 100%.

shown that the ORS-based method can clearly present the trend that the amplitudes of both the outer and inner race faults increase over the increasing speed. The analysed results using the *u*-axis vibration, *v*-axis vibration, and joint response can get consistent detections. In addition, the ORS-based method can distinguish two different motors under various running conditions, which indicates that Motor #2 presents more severe rolling bearing outer and inner race failures than Motor #1. Further, it is noted that the proposed joint responses based on the u-axis and v-axis vibrations can enhance the rolling bearing fault feature, thus detecting the rolling bearing faults with higher characteristic frequency amplitudes. It is validated that the proposed ORS method can achieve a more accurate and robust early fault diagnosis of the rolling bearing only using the traditional FFT algorithm.

4.3. *Hilbert envelope analysis*

The Hilbert envelope is a typical analysis method that can be used to demodulate the fault feature for the rolling bearing fault diagnosis.

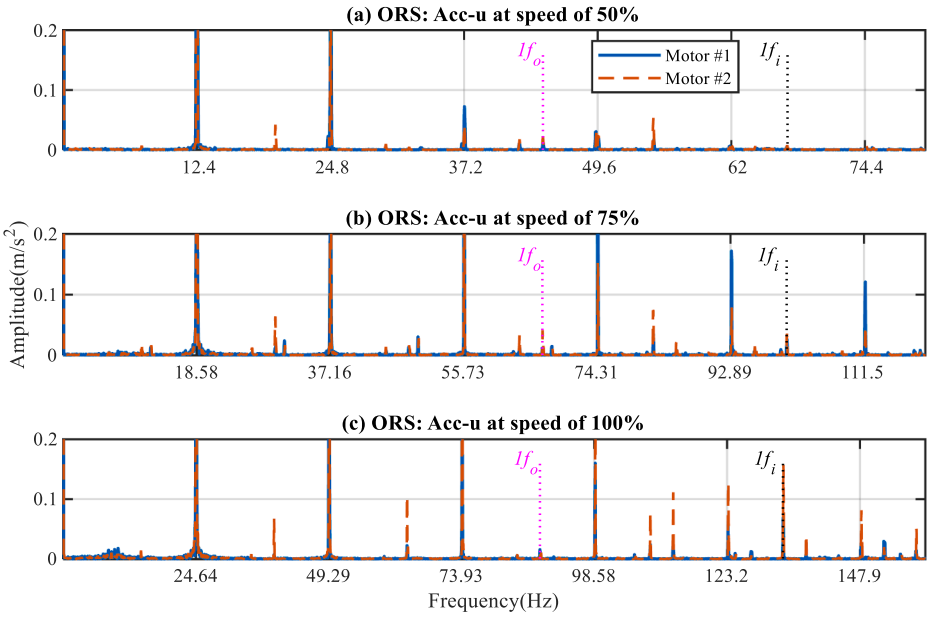

Fig. 20. Hilbert envelope spectrum based on the *u*-axis ORS vibration at (a) 50%, (b) 75%, and (c) 100%.

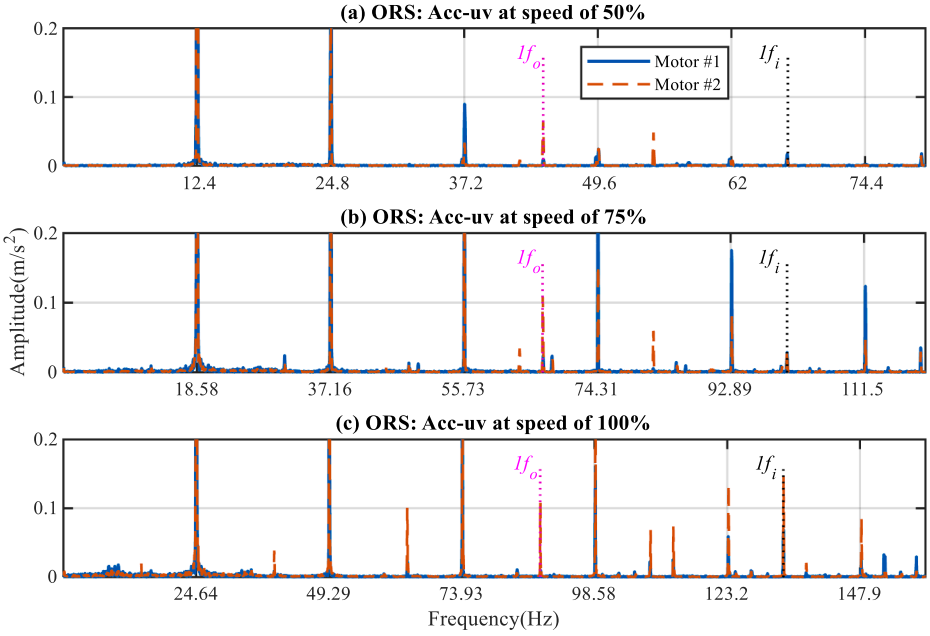

Fig. 21. Hilbert envelope spectrum based on the *u*-axis and *v*-axis ORS vibration at (a) 50%, (b) 75%, and (c) 100%.

Therefore, the Hilbert envelope analysis is adopted in this section to compare the OHS and ORS measurements for the rolling bearing fault detection. For the OHS-based envelope analysis, a variety of frequency bands are filtered out to compare the performance for the rolling bearing fault diagnosis, and finally the frequency band 1580–2620 Hz is selected as it can provide more excellent fault feature extraction. Similarly, the selected frequency band for ORS analysis is 0–200 Hz. Fig. 18 shows the envelope spectrum obtained by OHS using the collected vertical vibration signal. It is found that the rolling bearing faults cannot be fully detected, especially for cases in low-speed conditions. For example, the outer race fault of both two motors at 50 % speed and the outer and inner race faults at 75 % speed cannot be effectively identified. Based on the vertical and horizontal vibrations, Fig. 19 illustrates the calculated envelope spectrum under different load conditions. It can be seen that the joint response can slightly enhance the fault feature extraction, while the characteristic frequency at 50 % speed condition cannot be effectively extracted for the early fault diagnosis. It is believed that the lower SNR of the OHS measurement cannot ensure an accurate early fault diagnosis of the rolling bearing.

On the other hand, Fig. 20 displays the envelope spectrum obtained by ORS at the *u*-axis. It can be seen that the proposed ORS method can successfully extract the outer and inner race fault features under both low and high working speeds compared to the traditional OHS measurement. Additionally, Fig. 21 shows the envelope analysis based on the orthogonal outputs (*u* and *v* axes) of the ORS measurement. It is clear that the identified fault frequencies show higher amplitudes than that of using the single vibration signal, as shown in Fig. 20. It is validated that the ORS measurement can achieve the orthogonal measurements with higher SNR, which can facilitate a more convenient and robust Hilbert envelope analysis for the early rolling bearing fault diagnosis.

5. Conclusions

In this paper, a wireless triaxial ORS system is developed to improve the SNR of the vibration measurement and achieve an accurate and robust early fault diagnosis of the rolling bearing in the induction motor. The ORS system is designed to be installed on the rotating rotor of the induction motor to achieve the wireless vibration measurement with a maximum sampling frequency of 4000 Hz. Its theoretical deductions of the simple FFT and Hilbert envelope analysis for the early rolling bearing fault diagnosis are given in detail. The detection performance is tested by comparing it with the traditional OHS measurement using two induction motors with different degrees of rolling bearing faults. The time-domain analysis shows that the ORS system can significantly improve the SNR of the vibration measurement. It is validated that the simple FFT algorithm can sufficiently and accurately detect early rolling bearing faults compared to the traditional OHS system. In particular, the FFT analysis based on the orthogonal outputs can further enhance the outer and inner race fault features. In addition, it is demonstrated that the orthogonal outputs from the ORS system can help achieve a more convenient Hilbert envelope analysis for a more accurate fault diagnosis of the rolling bearing in the induction motor. It is believed that the developed ORS technology can facilitate the online diagnosis of the early rolling bearing fault thanks to signal acquisition with high SNR and simple and fast algorithm implementation.

In the future, we will work on the development of ORS with higher sampling frequency and wider detection range, which will lead to more stable signal acquisition and fault diagnosis. Moreover, more advanced signal processing methods based on the ORS measurement can be developed to achieve more effective and efficient early fault diagnosis of the rotating machine.

CRediT authorship contribution statement

Zuolu Wang: Methodology, Formal analysis, Investigation, Writing – original draft. **Dawei Shi:** . **Yuandong Xu:** Writing – review & editing. **Dong Zhen:** Conceptualization, Methodology, Validation. **Fengshou Gu:** Conceptualization, Formal analysis, Supervision. **Andrew D. Ball:** Writing – review & editing.

Declaration of Competing Interest

The authors declare that they have no known competing financial interests or personal relationships that could have appeared to influence the work reported in this paper.

Data availability

Data will be made available on request.

Acknowledgement

This research was supported by the National Natural Science Foundation of China (No. 5227053131, No. 52275101, and No. 52205099). The authors would like to express their appreciation to the Centre for Efficiency and Performance Engineering (CEPE) at the University of Huddersfield for supporting the experiments.

References

[1] H. Wei, Q. Zhang, M. Shang, Y. Gu, Extreme learning Machine-based classifier for fault diagnosis of rotating Machinery using a residual network and continuous wavelet transform, Measurement 183 (2021), 109864.
[2] X. Jiang, et al., Central frequency mode decomposition and its applications to the fault diagnosis of rotating machines, Mech. Mach. Theory 174 (2022), 104919.
[3] L. Wan, Y. Li, K. Chen, K. Gong, C. Li, A novel deep convolution multi-adversarial domain adaptation model for rolling bearing fault diagnosis, Measurement 191 (2022), 110752.
[4] X. Wang, J. Zheng, Q. Ni, H. Pan, J. Zhang, Traversal index enhanced-gram (TIEgram): A novel optimal demodulation frequency band selection method for rolling bearing fault diagnosis under non-stationary operating conditions, Mech. Syst. Sig. Process. 172 (2022), 109017.
[5] P. Gangsar, R. Tiwari, Signal based condition monitoring techniques for fault detection and diagnosis of induction motors: A state-of-the-art review, Mech. Syst. Sig. Process. 144 (2020), 106908.
[6] J. Cheng, Y. Yang, X. Li, J. Cheng, Adaptive periodic mode decomposition and its application in rolling bearing fault diagnosis, Mech. Syst. Sig. Process. 161 (2021), 107943.
[7] W. Kang, Y. Zhu, K. Yan, Z. Ren, D. Gao, J. Hong, Research on extracting weak repetitive transients of fault rolling element bearing, ISA Trans. 123 (2022) 381–397.
[8] S.J. Kim, et al., Motor-current-based electromagnetic interference de-noising method for rolling element bearing diagnosis using acoustic emission sensors, Measurement 193 (2022), 110912.
[9] H. Shi, Y. Li, X. Bai, K. Zhang, Sound-aided fault feature extraction method for rolling bearings based on stochastic resonance and time-domain index fusion, Appl. Acoust. 189 (2022), 108611.
[10] A. Choudhary, T. Mian, S. Fatima, Convolutional neural network based bearing fault diagnosis of rotating machine using thermal images, Measurement 176 (2021), 109196.
[11] Q. Han, Z. Ding, X. Xu, T. Wang, F. Chu, Stator current model for detecting rolling bearing faults in induction motors using magnetic equivalent circuits, Mech. Syst. Sig. Process. 131 (2019) 554–575.
[12] R. Yao, H. Jiang, Z. Wu, K. Wang, Periodicity-enhanced sparse representation for rolling bearing incipient fault detection, ISA Trans. 118 (2021) 219–237.
[13] R.B. Randall, J. Antoni, S. Chobsaard, The relationship between spectral correlation and envelope analysis in the diagnostics of bearing faults and other cyclostationary machine signals, Mech. Syst. Sig. Process. 15 (5) (Sep. 2001) 945–962, https://doi.org/10.1006/mssp.2001.1415.
[14] F. Pancaldi, R. Rubini, M. Cocconcelli, Time-varying metrics of cyclostationarity for bearing diagnostic, Mech. Syst. Sig. Process. 151 (Apr. 2021), 107329, https://doi.org/10.1016/j.ymssp.2020.107329.
[15] A. Marsick, H. André, I. Khelf, Q. Leclère, J. Antoni, Restoring cyclostationarity of rolling element bearing signals from the instantaneous phase of their envelope, Mech. Syst. Sig. Process. 193 (Jun. 2023), 110264, https://doi.org/10.1016/j.ymssp.2023.110264.
[16] P. Borghesani, The envelope-based cyclic periodogram, Mech. Syst. Sig. Process. 58–59 (Jun. 2015) 245–270, https://doi.org/10.1016/j.ymssp.2014.11.009.
[17] J. Antoni, G. Xin, N. Hamzaoui, Fast computation of the spectral correlation, Mech. Syst. Sig. Process. 92 (Aug. 2017) 248–277, https://doi.org/10.1016/j.ymssp.2017.01.011.
[18] S. Lu, Q. He, J. Wang, A review of stochastic resonance in rotating machine fault detection, Mech. Syst. Sig. Process. 116 (2019) 230–260.
[19] W. Zhang, P. Shi, M. Li, D. Han, A novel stochastic resonance model based on bistable stochastic pooling network and its application, Chaos Solitons Fractals 145 (2021), 110800.
[20] Y. Li, X. Liang, M. Xu, W. Huang, Early fault feature extraction of rolling bearing based on ICD and tunable Q-factor wavelet transform, Mech. Syst. Sig. Process. 86 (2017) 204–223.
[21] Y. Zhang, G. Ren, D. Wu, H. Wang, Rolling bearing fault diagnosis utilizing variational mode decomposition based fractal dimension estimation method, Measurement 181 (2021), 109614.
[22] J. Li, J. Tao, W. Ding, J. Zhang, Z. Meng, Period-assisted adaptive parameterized wavelet dictionary and its sparse representation for periodic transient features of rolling bearing faults, Mech. Syst. Sig. Process. 169 (2022), 108796.
[23] J. Antoni, G. Xin, N. Hamzaoui, Fast computation of the spectral correlation, Mech. Syst. Sig. Process. 92 (2017) 248–277.
[24] Z. Wang, J. Yang, H. Li, D. Zhen, F. Gu, A. Ball, Improved cyclostationary analysis method based on TKEO and its application on the faults diagnosis of induction motors, ISA Trans. (2021).
[25] L. Arebi, F. Gu, A. Ball, Rotor misalignment detection using a wireless sensor and a shaft encoder, University of Huddersfield, 2010.
[26] L. Arebi, F. Gu, A. Ball, A comparative study of misalignment detection using a novel Wireless Sensor with conventional Wired Sensors, in: Journal of Physics: Conference Series, IOP Publishing, 2012, p. 012049.
[27] L. Baghli, J.F. Pautex, S. Mezani, Wireless instantaneous torque measurement, application to induction motors, in: The XIX International Conference on Electrical Machines-ICEM 2010, IEEE, 2010, pp. 1–6.
[28] S. Jiménez, M.O. Cole, P.S. Keogh, Vibration sensing in smart machine rotors using internal MEMS accelerometers, J. Sound Vib. 377 (2016) 58–75.
[29] G. Feng, N. Hu, Z. Mones, F. Gu, A.D. Ball, An investigation of the orthogonal outputs from an on-rotor MEMS accelerometer for reciprocating compressor condition monitoring, Mech. Syst. Sig. Process. 76 (2016) 228–241.
[30] Y. Xu, et al., Orthogonal on-rotor sensing vibrations for condition monitoring of rotating machines, J. Dynam., Monit. Diagnost. 1 (1) (2021) 29–36.
[31] Y. Xu, G. Feng, X. Tang, S. Yang, F. Gu, and A. D. Ball, 'A Modulation Signal Bispectrum Enhanced Squared Envelope for the detection and diagnosis of compound epicyclic gear faults', Struct. Health Monit., p. 14759217221098576, 2022.
[32] W. Zhao, et al., Research on rolling bearing virtual-real fusion life prediction with digital twin, Mech. Syst. Sig. Process. 198 (Sep. 2023), 110434, https://doi.org/10.1016/j.ymssp.2023.110434.
[33] K. Feng, W.A. Smith, R.B. Randall, H. Wu, Z. Peng, Vibration-based monitoring and prediction of surface profile change and pitting density in a spur gear wear process,

Mech. Syst. Sig. Process. 165 (Feb. 2022), 108319, https://doi.org/10.1016/j.ymssp.2021.108319.
[34] K. Feng, J.C. Ji, Y. Zhang, Q. Ni, Z. Liu, M. Beer, Digital twin-driven intelligent assessment of gear surface degradation, Mech. Syst. Sig. Process. 186 (Mar. 2023), 109896, https://doi.org/10.1016/j.ymssp.2022.109896.
[35] Y. Zhang, et al., Digital twin-driven partial domain adaptation network for intelligent fault diagnosis of rolling bearing, Reliab. Eng. Syst. Saf. 234 (Jun. 2023), 109186, https://doi.org/10.1016/j.ress.2023.109186.
[36] K. Kumar, S. Shukla, S.K. Singh, A combined approach for weak fault signature extraction of rolling element bearing using Hilbert envelop and zero frequency resonator, J. Sound Vib. 419 (2018) 436–451.
[37] M.B. Abd-el-Malek, A.K. Abdelsalam, O.E. Hassan, Novel approach using Hilbert Transform for multiple broken rotor bars fault location detection for three phase induction motor, ISA Trans. 80 (2018) 439–457.
[38] M. Xu, Y. Shao, Y. Han, F. Gu, A. Ball, A Numerical Analysis of Internal Radial Clearances on Affecting Vibration of Rolling Element Bearings with Local Defects, in: International Conference on Maintenance Engineering, Springer, 2020, pp. 1–13.
[39] M. Xu, G. Feng, Q. He, F. Gu, A. Ball, Vibration characteristics of rolling element bearings with different radial clearances for condition monitoring of wind turbine, Appl. Sci. 10 (14) (2020) 4731.